Simulation for stability of a beam-mass based high-resolution MEMS gravimeter

Ye, Guigen ; Fan, Xuejun; Middelburg, Luke M.; El Mansouri, Brahim; Poelma, René H.; Zhang, Guoqi

Citation (APA)
Ye, G., Fan, X., Middelburg, L. M., El Mansouri, B., Poelma, R. H., & Zhang, G. (2022). Simulation for stability of a beam-mass based high-resolution MEMS gravimeter. *Materials and Design*, *219*, Article 110788. https://doi.org/10.1016/j.matdes.2022.110788
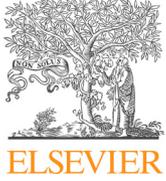
Important note
To cite this publication, please use the final published version (if applicable).
Please check the document version above.

Simulation for stability of a beam-mass based high-resolution MEMS gravimeter

Guigen Ye [a], Xuejun Fan [b,c,*], Luke M. Middelburg [c], Brahim El Mansouri [c], René H. Poelma [c], Guoqi Zhang [c,*]

[a] Department of Engineering Mechanics, China University of Petroleum (East China), Qingdao, China
[b] Department of Mechanical Engineering, Lamar University, Beaumont, TX 77710, USA
[c] Department of Microelectronics, Delft University of Technology, Delft, the Netherlands

HIGHLIGHTS

- Stability and mechanistic simulations for a MEMS gravimeter are conducted.
- General principles for the improvement of relative gravimeter are explained.
- Three distinct deformation modes of a 4-beam-mass MEMS system are identified.
- The mode with buckling present a very sensitive and unstable region.
- The mode without buckling and zero-stiffness provide a stable low resonance frequency.

GRAPHICAL ABSTRACT
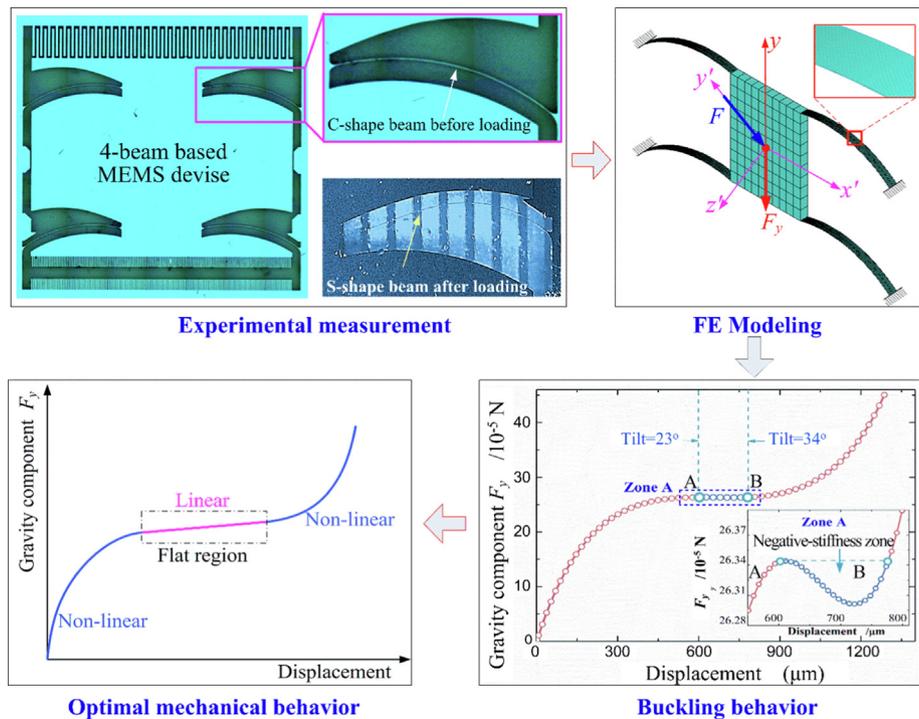
ARTICLE INFO

ABSTRACT

In this paper, stability and mechanistic simulations for a four-beam-mass-based MEMS gravimeter were conducted, and guidelines for the gravimeter design were proposed. Based on a prototyped MEMS device, the nonlinear finite element model was validated first against the experimental results. Then, we demonstrated three different scenarios in design that have three distinct modes of deformation: the mode with buckling (case 1), the mode without buckling but with a single zero-stiffness point (case 2), and the mode

* Corresponding authors at: Department of Mechanical Engineering, Lamar University, Beaumont, TX 77710, USA.
 E-mail addresses: xuejun.fan@lamar.edu (X. Fan), G.Q.Zhang@tudelft.nl (G. Zhang).

without both buckling and zero-stiffness point (case 3). Both case 1 and case 2 presented an unstable and sensitive region, in which a tiny perturbation could result in a rapid increase of the resonance frequency. Case 3, on the other hand, could provide a stable and low resonance frequency with a linear relationship between the displacement and gravitational acceleration. An optimized design of a beam/spring-mass-based relative gravimeter could be achieved using the above guidelines.

1. Introduction

Monitoring of Earth's gravitational field is of great significance in many applications, such as the detection of hidden hydrocarbon reserves, groundwater monitoring, magma build-up before volcanic eruptions, geophysical mapping of sub-surface voids and sinkholes, earthquake predictions, etc. [1–4]. There are two broad categories of gravimeters: absolute and relative gravimeters. An absolute gravimeter is designed based on measuring the time of a mass falling over a given distance. A relative gravimeter operates by measuring the "change" in the displacement of a spring/beam system. The absolute gravimeter can reach high resolution and accuracy but is usually bulky, heavy, and expensive. The microelectromechanical-systems (MEMS) based relative gravimeter provides a potential solution for achieving ultra-high accuracy and sensitivity in addition to the advantages of mass production and miniaturization [5–7]. Relative gravimeters can also measure static gravity acceleration for specific positions as well as the detection of dynamic gravity changes with time at a given location [8,9].

A MEMS-based gravimeter usually consists of a spring/beam-mass system for enhanced sensitivity to external mechanical disturbance (gravitational force) [10,11]. Near-zero and even negative stiffness can be achieved for such a system that deforms with buckling. Therefore, the buckled spring/beam-mass system was adopted to reach an ultra-high-resolution [12]. Cella et al. [13] studied the low-frequency behaviour of a geometric antispring (GAS). They identified the bistability (buckling) behaviour, which is a natural result of the compression of the spring related to its arc length. With a couple of folding singularities, a near-zero resonance frequency was obtained. Middlemiss et al. [14,15] further fabricated a MEMS gravimeter using a novel three-flexure antispring system, and the resonance frequency can be reduced to 2.3 Hz with an acceleration sensitivity of 40 ng/Hz$^{1/2}$. This MEMS gravimeter was further developed by Prasad et al. [16] to reach an acceleration sensitivity of about 8 ng/Hz$^{1/2}$, which was integrated on a small platform with automated temperature control and manually adjustable tilt option.

Buckling is an instability phenomenon, in which the system jumps from one stable state to another stable state. For this reason, some other MEMS-based gravimeters were designed to prevent buckling. Droogendijk [17] designed a bulk-micromachined gravitational accelerometer avoiding buckling. Li et al. [18] presented a MEMS device based on a novel capacitive readout scheme, which achieved an acceleration sensitivity of 30 ng/Hz$^{1/2}$. A linear spring system with a resonance frequency of 13.2 Hz was used without buckling over the entire deflection range. Recently, Tang et al. [6,19] designed a MEMS gravimeter with an acceleration sensitivity of 8 ng/Hz$^{1/2}$ at bandwidth of 1 Hz. The device included a curved beam and two folded beams. The combination of these three beams led to a quasi-zero positive stiffness behaviour with an ultra-low resonant frequency of 3.0 Hz. Wu et al. [20] proposed a spring-mass structure that could achieve the lowest resonance frequency of 0.7 Hz by improving the spring's compliance with a negative-stiffness compensation mechanism induced by axial force.

It can be noted from the above analysis that, some devices utilized the buckling behaviour to achieve ultra-low resonance frequency, while others attempted to prevent the buckling. It is still unclear what kind of the deformation mode of a spring/beam-mass system would provide the best solution for the MEMS gravimeter design to achieve a stable and ultra-low resonance frequency. In our recent work [21], we presented a high-resolution MEMS gravimeter based on a four-beam-mass system. The lowest resonance frequency of 8.7 Hz was measured at the tilt angle of 34°. Moreover, the MEMS gravimeter used an integrated capacitive transducer and an impedance readout chip. The achievable acceleration sensitivity was 17.02 ng/Hz$^{1/2}$. However, there is no analysis of why the device deforms excessively after a tilting angle of 34°.

In this paper, detailed modeling of buckling/non-buckling mechanistic behaviour was performed based on our fabricated four-beam-mass MEMS system. The models were validated first against the measurements in terms of the system's resonance frequency. Subsequent detailed parametric studies of small variations in geometrical design revealed three distinct deformation modes, with or without the presence of buckling. In what follows, the fabrication and measurements of this four-beam-mass based gravimeter are briefly described in Section 2. The nonlinear finite element model and the comparison with the experimental results are discussed in Section 3. In Section 4, the detailed analysis of the three different modes of deformation is presented, and the general principles for the improvement of the structural design of a relative gravimeter are further explained. The conclusions of this work are given in Section 5.

2. Device fabrication and measurements

2.1. Device fabrication

A four-beam-mass system was proposed and prototyped [21]. The process flow is schematically shown in Fig. 1. The fabrication was based on silicon bulk micromachining of four-inch p-type (boron doped) substrate. As the capacitive read-out transducer was also fabricated from the same substrate, a so-called trench isolation technique was employed. The trenches of 100 μm were etched by deep reactive ion etching (DRIE), where the patterned silicon oxide was used as a masking layer (see Fig. 1(a)). The etched trenches were illustrated in Fig. 1(b). These trenches were then filled with silicon nitride by low pressure chemical vapor deposition (LPCVD), as shown in Fig. 1(c). The electrical isolation of different parts of the substrate was completed in the process by a backside etch by a DRIE process, while landing on the filled trenches. After patterning the contact openings in the silicon nitride layer, an aluminum layer of 1 μm was deposited and patterned using lithography and standard dry-etching techniques to form the metal interconnects, as illustrated in Fig. 1(d). Subsequently, the masking layers were patterned by lithography and
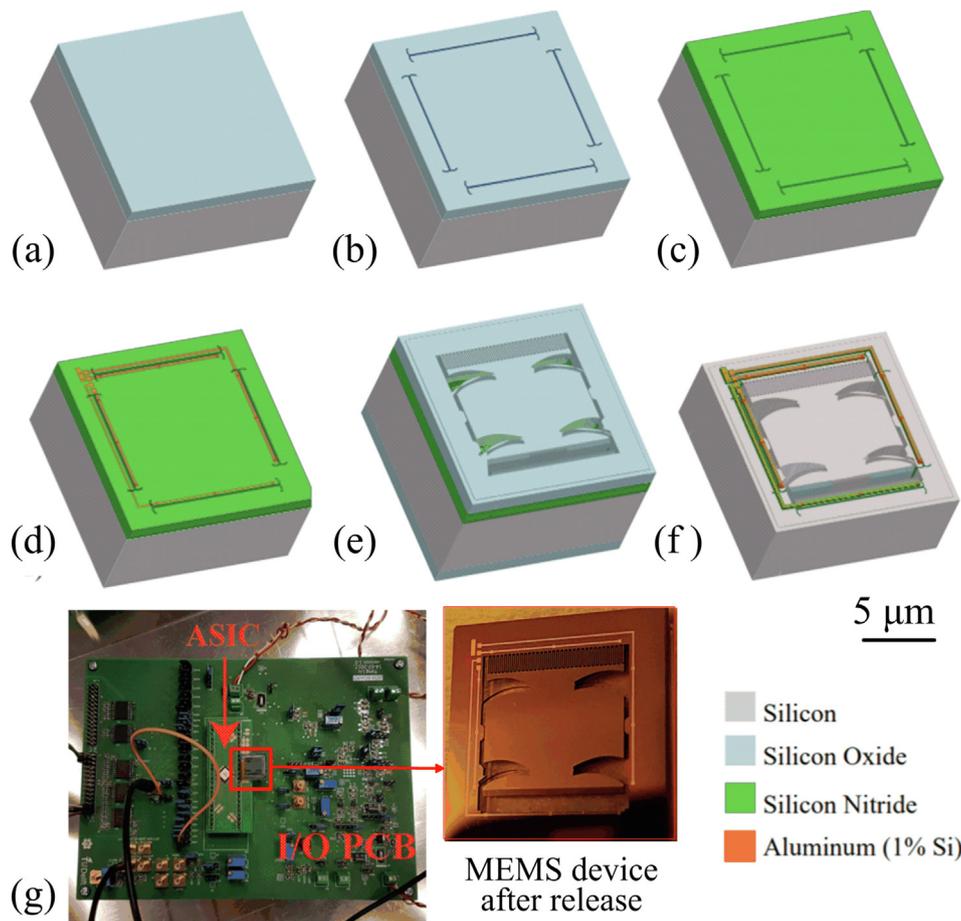
Fig. 1. Process flow of the MEMS device: (a) hard mask, (b) trench patterning, (c) trench filling with Si$_3$N$_4$, (d) metal interconnects, (e) mass/beam patterns, (f) released device, (g) packaged device [21].

plasma etching. The transducer structure was finally defined by a through-wafer etch from front to backside. Fig. 1(e) shows the resulting structure. Vapor hydrofluoric (HF) acid was then employed to release the devices, while halo-structures of excess substrate material were removed from the devices (Fig. 1(f)). In order to minimize parasitic impedance, the packaged dies were directly wire-bonded on the PCB that houses the high-resolution capacitive read-out circuitry. The packaged device was shown in Fig. 1(g). For the above-mentioned manufacturing process, beams and mass were made from the silicon wafer of 300 μm thickness.

2.2. Resonance frequency measurement

Fig. 2(a) gives the optical microscope image of our fabricated beam-mass device. A center mass was supported by four identical slender "C-shape" beams. The configuration with four curved beams can increase the rotational stiffness, and also can make the design more compact, which ensured that the beams had a certain length to deform with low stiffness. A "stopper" was designed to prevent excessive displacement which might lead to catastrophic damage. To measure the system's resonance frequency, the device was placed in a mechanical shaker under varying tilt angles, from 0° to 90°, as shown in Fig. 2(b). The initial measuring position was in a horizontal position with a 0° tile angle. The mechanical excitation in y' direction (perpendicular to the ground pale (x'-z') was then applied with a spectrum of frequencies at each

tilt angle, and the spectral location of resonance was then detected by a dramatic increase in capacitive response.

A mechanical shaker (Brüel & Kjaer 4810) was used to deliver a sinusoidal signal in the frequency range between 1 Hz and 20 Hz. Fig. 3(a) plotted the measured mechanical spectrum of the device at different tilt angles. In Fig. 3(a), the maximum magnitude of the signal for each curve corresponded to the point of resonance. Fig. 3(b) plotted the resonance frequency as a function of tilt angle. The resonance frequency decreased almost linearly with the tilt angle from 23° to 34°. Thus, the resonance frequency, as well as the mechanical sensitivity, of the device were tuneable by varying the tilt angle. From these measurements, the lowest measured resonance frequency equals 8.7 Hz for a tilt angle of 34°. Based on a sensitivity and noise analysis, the input-referred system acceleration sensitivity was obtained of 17.02 ng/Hz$^{1/2}$ [21].

When the tilt angle was below 23°, the resonance frequency of the device was greater than 20 Hz, which was outside of the shaker's range. Thus, no resonance signal was recorded. When the tilt angle reached to 35°, the center mass moved excessively and snaped through and hit the stopper. The beam became a "S-Shape" from the original "C-Shape", indicating buckling occurred, as shown in Fig. 4. In the original design, the tilt angle until 90° to a vertical direction was desired. However, due to the variability in manufacturing, the dimensions of the prototyped device led to buckling at the tilt angle of 35°. In the next section, a detailed finite element analysis was performed to investigate the sensitivity to geometry variation.
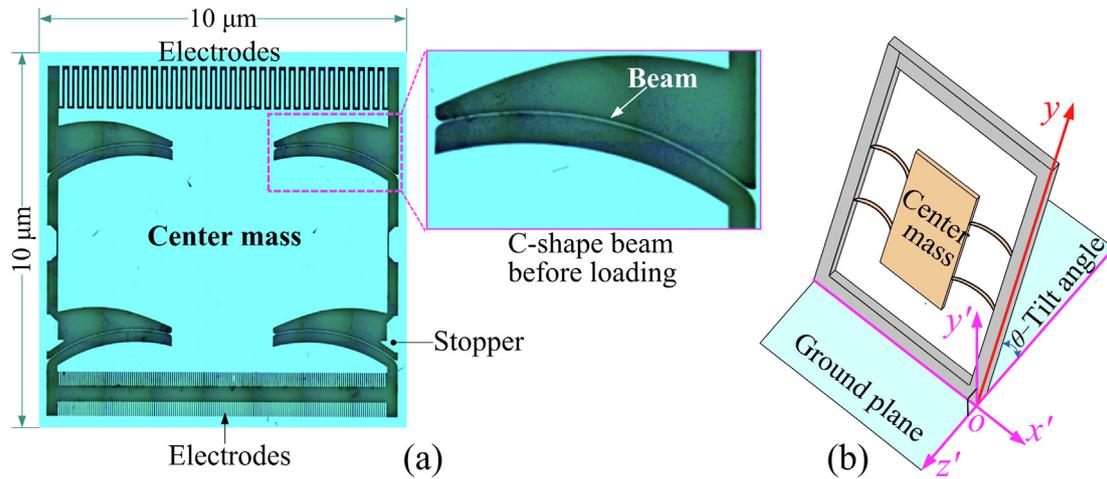
Fig. 2. (a) Optical microscope image of the fabricated MEMS device, (b) schematic of the MEMS device with a tilt angle θ.
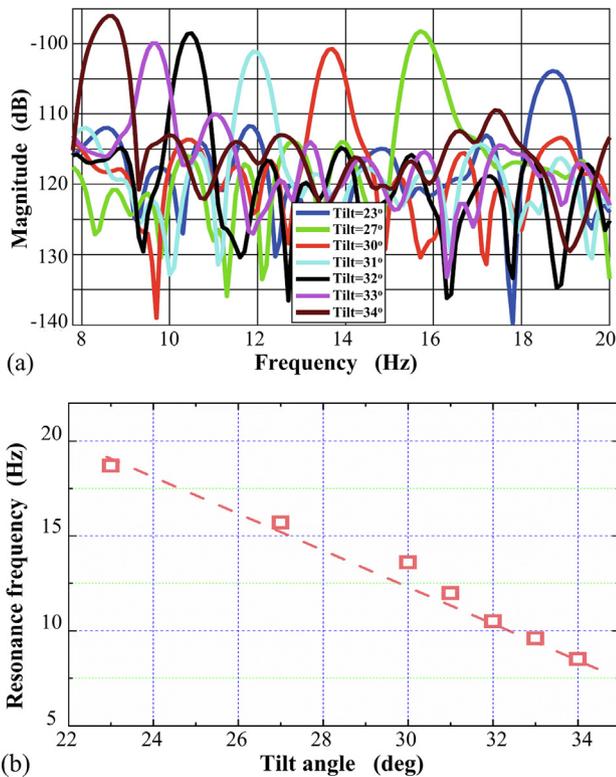

Fig. 3. Measured results for tilt angle ranging from 23° to 34°: (a) mechanical spectrum of the device, (b) resonance frequency [21].
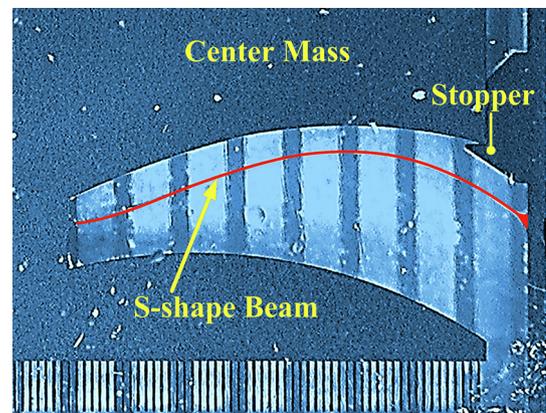

Fig. 4. Image of the buckled beam at tilt angle of 35° (the beam is highlighted by a red line). (For interpretation of the references to colour in this figure legend, the reader is referred to the web version of this article.)

3. Finite element modeling

There were four geometrical design parameters: radius (R), height (h), inclination angle (α), and sector angle (β) to define the geometry of the curved beam, as shown in Fig. 5(a). Table 1 gives these geometrical parameters based on the measurements from the final fabricated device. In Table 1, two additional sets of design parameters, which were used in the subsequent section, were also presented. Table 2 gives the elastic material properties of the bulk silicon wafer [22]. The x and y axes indicated in Table 2 represented $\langle 100 \rangle$ direction, while the z-axis indicated [100] direction of the silicon wafer.

Finite element software ANSYS (version 19.0) was used to model the device. In our study, we used beam element (line element) for the curved beams, and shell element (area element) for the center mass. The center mass was simplified into a rectangular plane and treated as a rigid body (very high modulus). In this model, the beam and shell elements shared the same node at the junction. Both the beam element and shell element have six degrees of freedom at each node, therefore the beam and shell elements can be perfectly connected without any additional treatment. The shell element (Shell281) had a thickness of t, and the beam elements (Beam189) had the thickness and height as t and h, respectively. Fig. 5(b) showed the geometry model used in ANSYS, and Fig. 5(c) showed the visualized "3D" finite element model.

The gravity force ($F = mg$) was applied on the center mass in the negative y' direction (perpendicular to the ground pale (x'-z'), see Fig. 5(c)). When a tilt of the center mass surface (x'-y plane) with respect to the ground plane was applied from 0° to 90° (from horizontal to vertical), the resulting gravity component in the negative y-direction was $F_y = mg\sin\theta$. This gravity component acted on the center mass to produce the prestress on the beams. By doing so, the stiffness and resonance frequency changed accordingly. During the simulation, the deformations of the beams were predicted with arc-length method to capture a complete buckling phenomenon [23].
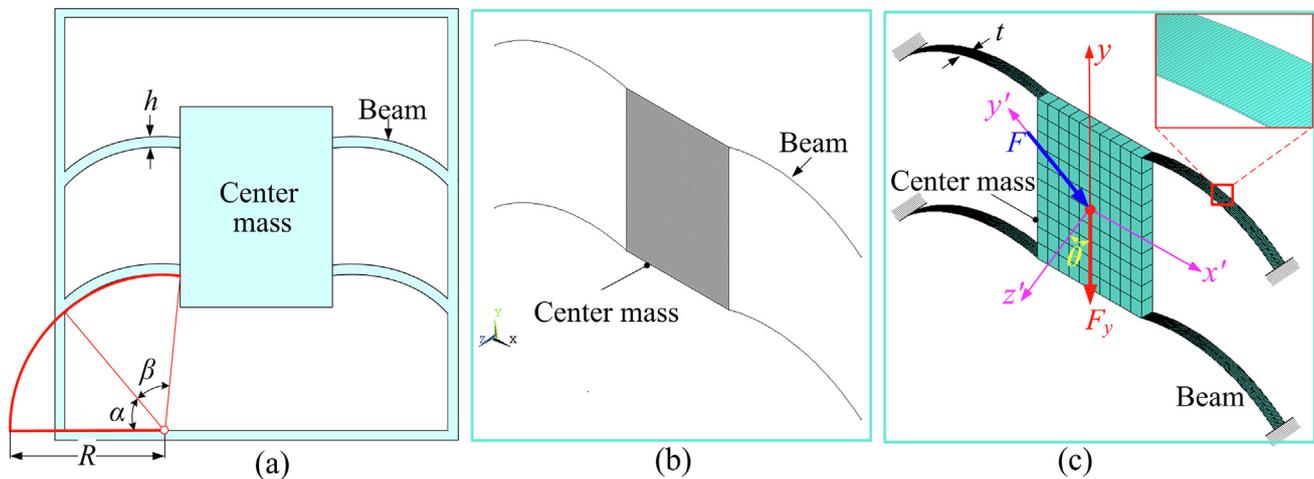
Fig. 5. (a) Geometry of the four-beam-mass system, (b) geometric model used for simulation, (c) finite element model showing the cross-section of the beams and the thickness of the shell.

Table 1
Measured and simulated parameters for the beam-mass structure.

Quantity	Symbol	Measured Value (Simulation Case 1)	Simulation Case 2	Simulation Case 3
Mass	m	45.95 mg	45.95 mg	45.95 mg
Beam height	h	4.86 μm	4.86 μm	4.86 μm
Beam radius	R	4000 μm	4000 μm	4000 μm
Inclination angle	α	50.3°	50.3°	50.3°
Sector angle	β	54.1°	54.3°	55.0°
Beam thickness	t	300 μm	300 μm	300 μm

Table 2
Anisotropic elastic properties of the bulk silicon wafer [22].

Elastic properties	Value
Young's modulus	$E_x = E_y = 169$ GPa, $E_z = 130$ GPa
Poisson ratio	$\mu_{xz} = \mu_{zx} = 0.36$, $\mu_{yz} = \mu_{zy} = 0.28$, $\mu_{xy} = \mu_{yx} = 0.064$
Shear modulus	$G_{yz} = G_{zx} = 79.6$ GPa, $G_{xy} = 50.9$ GPa

Mesh sensitivity was studied first using the tilt angle of 90° when the device was placed vertically with respect to the ground. The displacement was caused by the weight of the center mass. Fig. 6 plotted the maximum displacement of the center mass with the number of beam elements in each beam. It can be seen that the displacement of the center mass was about 1300 μm. Such large displacement indicated the occurrence of buckling, and also
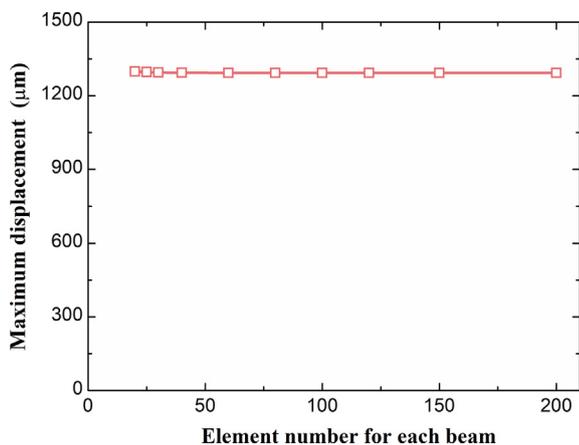

Fig. 6. Displacement of the center mass versus the element number in each beam.

implied that the complete buckling behaviour can be captured. It also can be seen from Fig. 6 that, with using the quadratic element Beam189, convergence results can be achieved even with less than 50 elements in each beam. Nevertheless, in this study, each beam was divided into 200 elements to eliminate possible numerical errors in buckling analysis.

Next, the system's mechanical behaviour as a function of tilt angle was studied. Fig. 7(a) gave the center mass displacement versus tilt angle, and the corresponding force–displacement curve was shown in Fig. 7(b). From Fig. 7(a) the beams experienced a large nonlinear deformation before they lost stability at 35°. When the tilt angle exceeded 35°, the displacement jumped from 600 μm to 780 μm immediately, indicating the occurrence of buckling. The system jumped from one unstable state (Point A) to another stable (Point B). In Fig. 7(c), it clearly showed the beams changed from the original "C-shape" to "S-shape". The threshold tilt angle of 35° predicted from the simulation was remarkedly in accordance with the experimental results.

Third, the modal analyses considering the gravity-caused pre-stress were further carried out. Fig. 8 presented the first-order mode at different tilt angles. It was found that the first-order mode for different tilt angles was symmetric at each tilt angle. The deformation mode always corresponded to translation along the main axis of the device (y-axis in Fig. 5(c)). It also can be found that there was little difference in amplitude at different tilt angles, but the equilibrium position got lower at a larger tilt angle since the deformation of the beams increased with the tilt angle. Fig. 9 further plotted the simulated and measured resonance frequencies at different tilt angles. The simulated resonance frequencies matched well with the measured ones, with a maximum error of 8% at 34°. The excellent agreement validated the simulation approach and the finite element model used for this system. In the next section, we used the finite element model to investigate the different modes of deformation for such a beam-mass system.
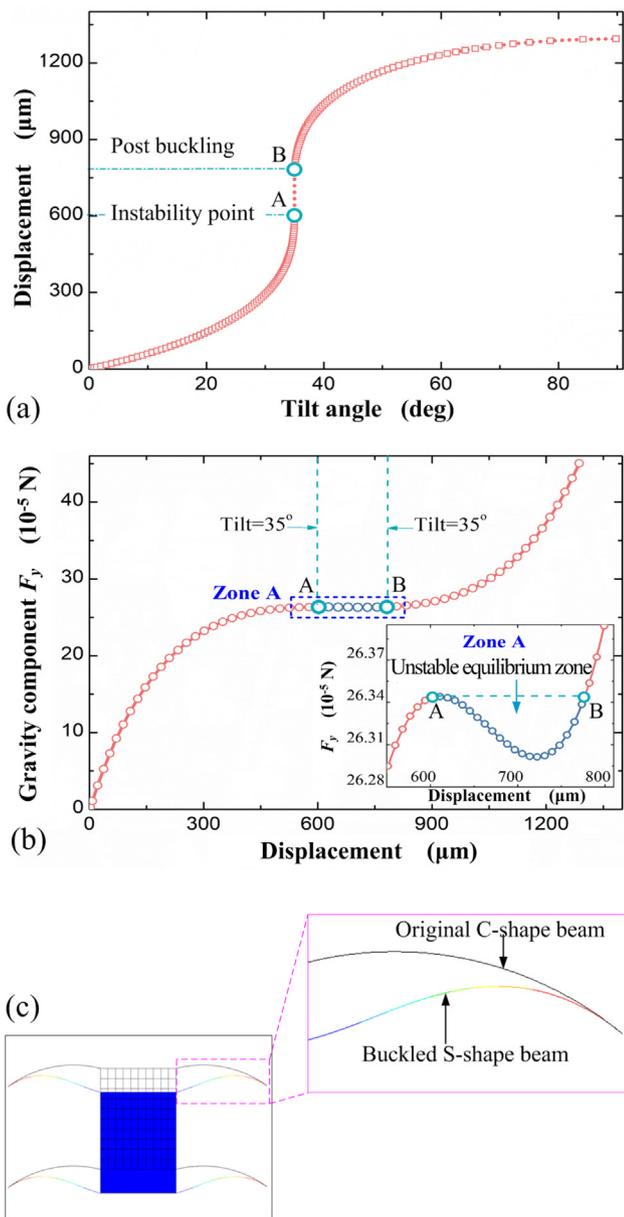
Fig. 7. (a) Center mass displacement evolving with tilt angle, (b) the gravity component F_y ($F_y = mg\sin\theta$, g = 9.800 m/s², θ = 0°-90°) evolving with displacement, (c) the deformed beam obtained at θ = 35°.

4. Three modes of deformation

To investigate the mechanical stability of the four-beam-mass structure, three cases were considered, as shown in Table 1. The geometry of case 1 was measured from the actual device. In these three cases, only the sector angle was changed from 54.1° to 55°, while other parameters remained the same. Three typical deformation modes were identified. When the sector angle was 54.1° (case 1, same as the fabricated device geometry), the buckling behaviour was observed. As the sector angle increased to 54.3° (case 2), there was a zero-stiffness point without buckling. And when the sector angle further increased to 55.0° (case 3), there existed a region in which the beam deformed with a stable (positive) near-zero-stiffness. The geometric structures of these three cases had no noticeable differences, as shown Fig. 10. However, such a small difference would result in three distinct modes of deformation.

4.1. Buckling and non-buckling

The displacement against tilt angle for cases 1, 2, and 3 were shown in Fig. 11(a)–(c), and the corresponding force–displacement curves were shown in Fig. 11(d)–(f). For case 1, buckling occurred at 35°, following an "unstable equilibrium" zone as the tilt angle exceeded 35° (see Fig. 11(d)), at which the instability took place and the displacement jumped from 600 μm to 780 μm (Fig. 11 (a)). The system "jumped" into a post-buckling stable zone, and the system restored the stiffness.

In case 2, no "snap-through" behaviour of the displacement was observed, but a zero-stiffness point was achieved at 34.75° (Fig. 11 (b) and (e)), with which an ultra-low resonance frequency can be obtained. The displacement showed a highly nonlinear dependency on the gravity component near the zero-stiffness point. In this highly nonlinear region, the ratio of the displacement increment to the gravity variation was not constant (because of the non-linearity) and depended on the deflection, to be discussed in the next sub-section (section 4.2).

For case 3, the force always increased with the displacement with a positive slope (see Fig. 11(f)). The displacement increased with the tilt angle nonlinearly from 0° to 32.1°, with relatively large stiffness. There existed a zone (Zone A) in the range of 32.1–33.1°, with a relatively near-zero stiffness. From the enlarged figure illustrated in Fig. 11(f), a linear relationship between the force and displacement was obtained in the displacement range of 600 −710 μm, corresponding to a tilt range of 32.4–32.8°. This means a stable (positive) stiffness and resonance frequency can be achieved in this region.
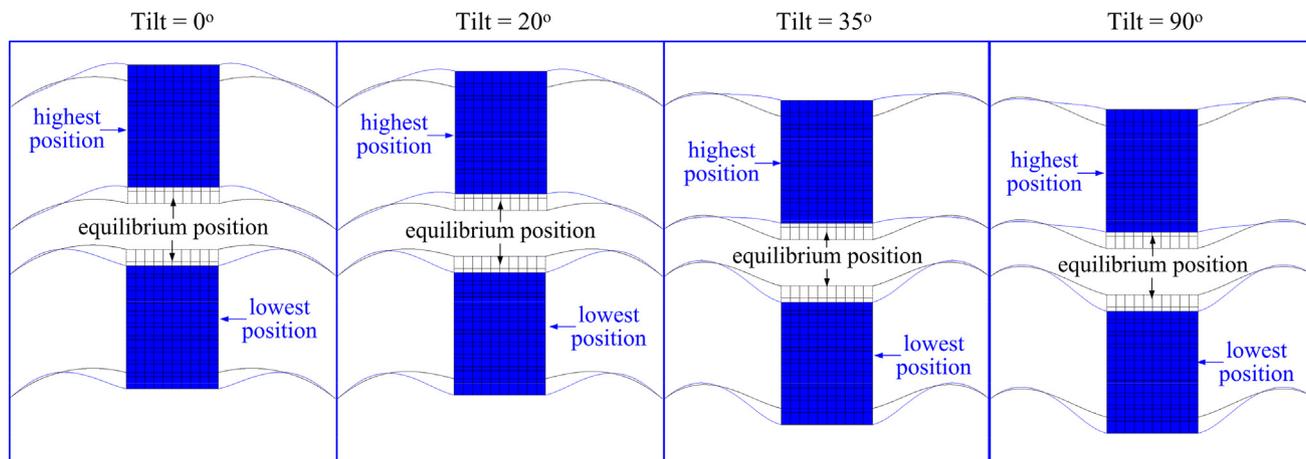

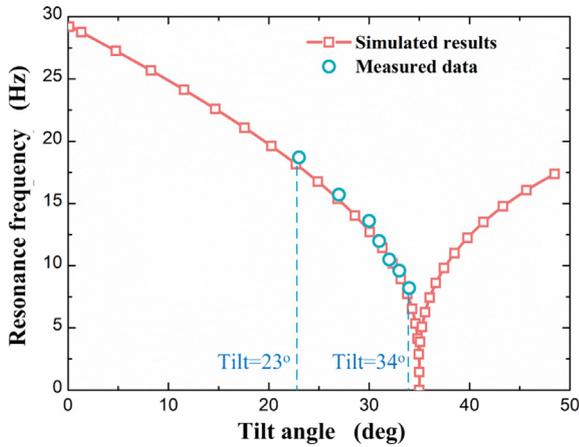
Fig. 8. First-order mode at different tilt angles.

Fig. 9. Comparison of the simulated resonance frequency with measured results at different tilts.

4.2. Stability of the resonance frequency

Fig. 12 presented the resonance frequency of the system evolving with tilt angle. From Fig. 12(a) for case 1, in a region near the

instability point (35°), the resonance frequency was very sensitive to the tilt angle, i.e., a very small change of the tilt angle could result in a significant variation of the resonance frequency. Because of this sensitive zone, a tiny design/fabrication deviation could result in a quite different resonance frequency. For example, for the device which is designed with a working resonance frequency of 0.5 Hz, a 1% fabrication deviation of the center mass would make the resonance frequency increase by ∼1000%. Therefore, the ultra-low resonance frequency near the instability point is very sensitive to the variations of many parameters including gravity variation. The device should not be designed to work in this region.

As for case 2, even though buckling did not occur, in a region right near the zero-stiffness point, there still existed a sensitive zone (Fig. 12(b)), where the resonance frequency changes rapidly with the tilt angle: only a 0.5° variation of the tilt angle resulted in a 6 Hz variation of the resonance frequency. Therefore, the device should not be designed to work in this region despite a near-zero resonance frequency.

Fig. 12(c) plotted the evolution of the resonance frequency for case 3. With the design parameters provided in Table 1, the lowest resonance frequency of 3.3 Hz can be achieved at 32.65°. However, different from case 1 and case 2, the resonance frequency changed smoothly and slightly near the lowest resonance frequency point, and it was almost unchanged in the range of 32.4–32.8°, indicating
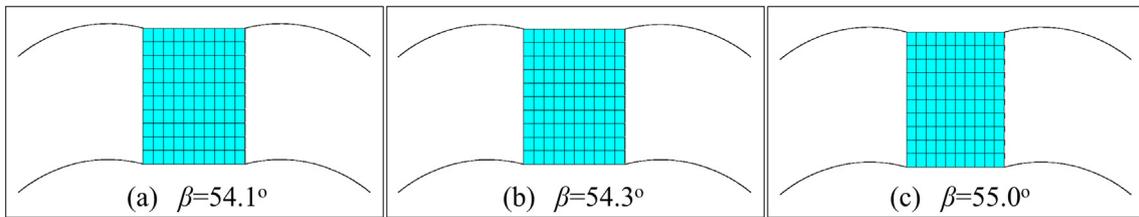

Fig. 10. Beam-mass structure for: (a) case 1 β = 54.1°, (b) case 2 β = 54.3° and (c) case 3 β = 55.0°.
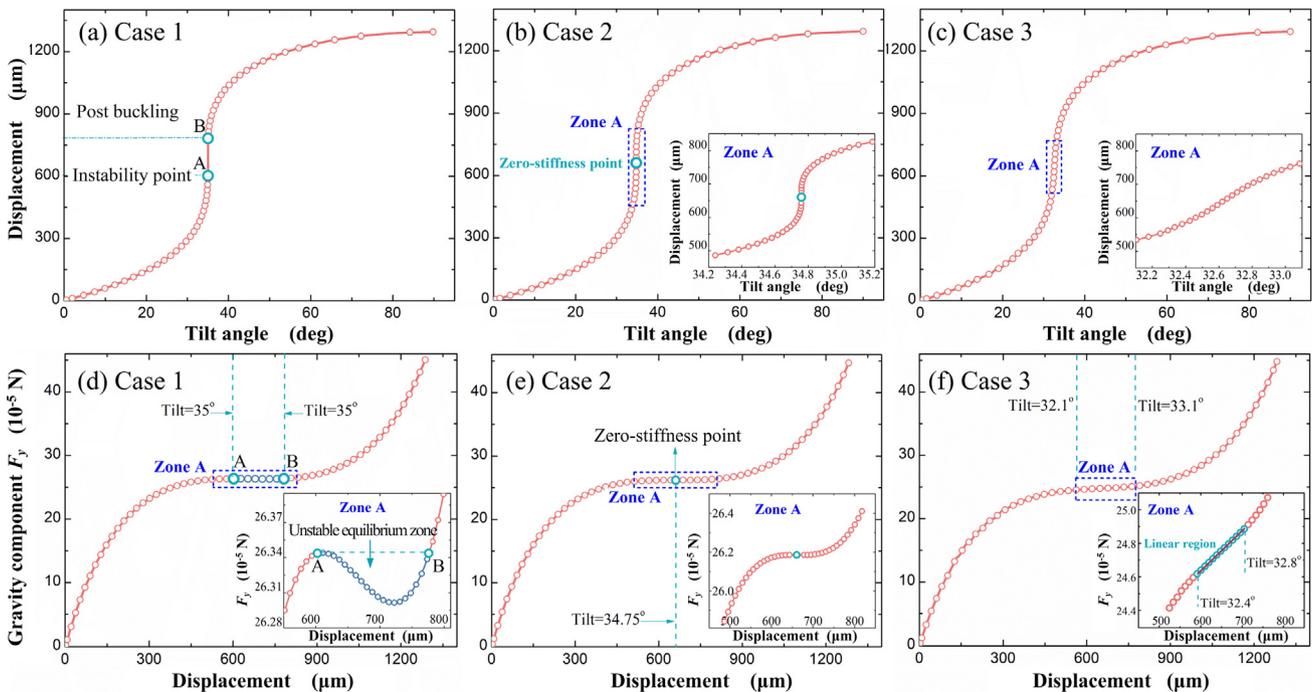

Fig. 11. The displacement of center mass evolving with tilt angle for: (a) case 1, (b) case 2, (c) case 3, and the gravity component F_y (F_y = $mg\sin\theta$, g = 9.800 m/s^2) evolving with displacement for: (d) case 1, (e) case 2 and (f) case 3.

that a stable resonance frequency can be achieved in this region. It is worth noticing that the frequency-tilt curve is upward-concave at the lowest resonance frequency point (see the enlarged figure illustrated in Fig. 12(c)), which means a stable state can be achieved at the extreme point (32.65°). This is different from case 1 and case 2, where the frequency-tilt curve is always downward-concave (see Fig. 12(a) and Fig. 12(b)), indicating an unstable status.
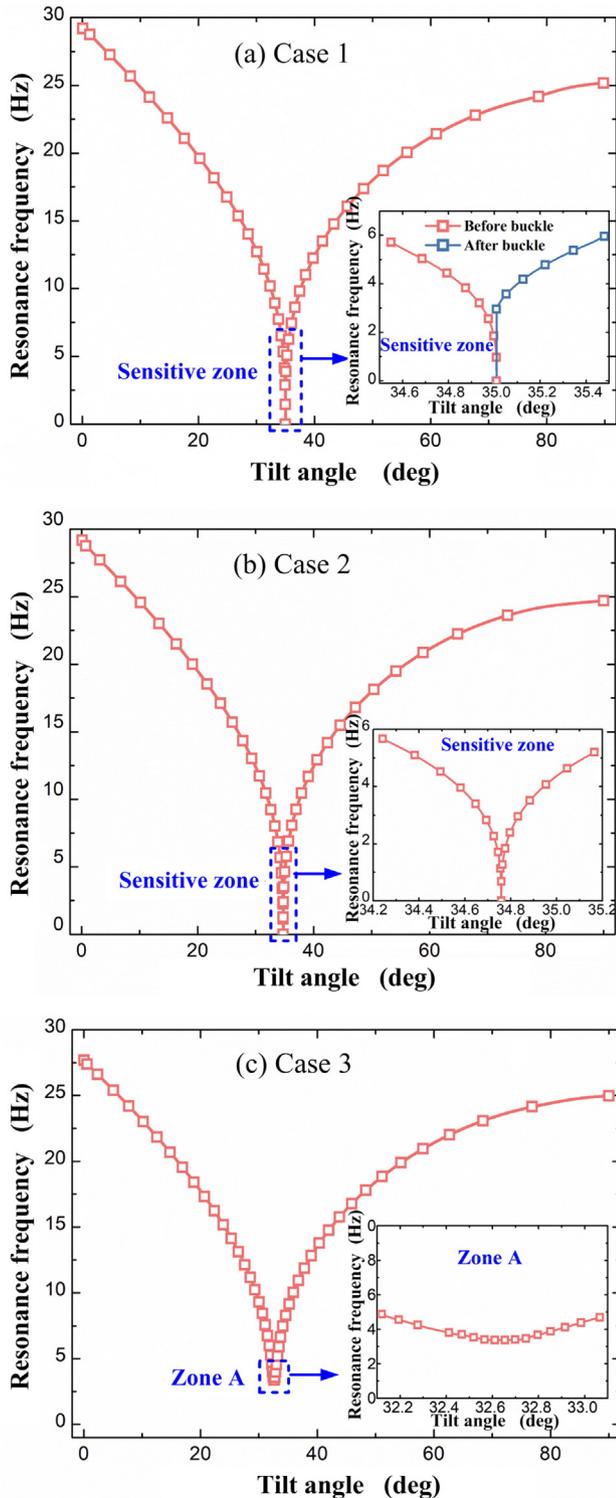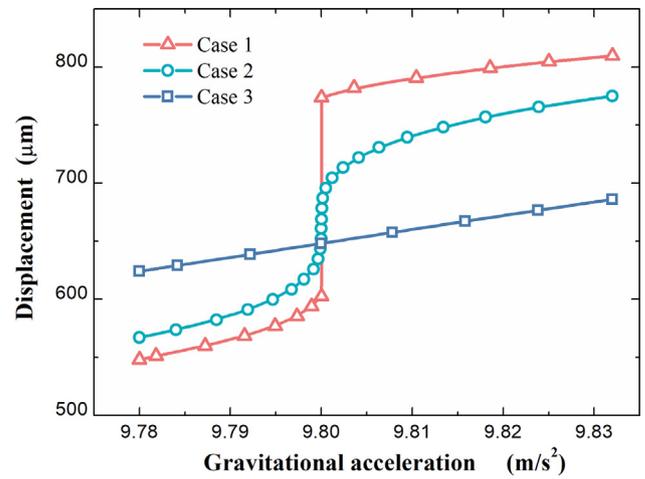

Fig. 13. Displacement plotted with gravitational acceleration (with g = 9.800 m/s² as a standard case).
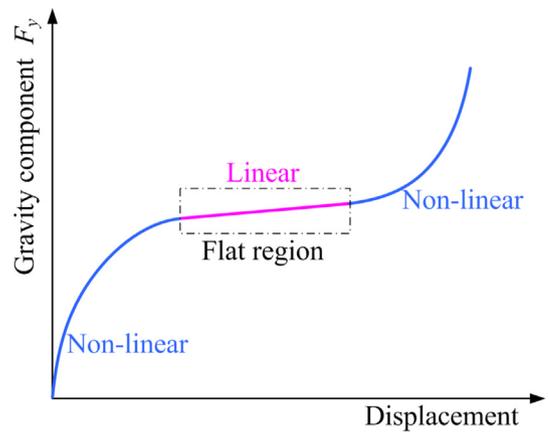

Fig. 14. Schematic force–displacement curve of the optimized beam-mass structure.

4.3. Relation between displacement and gravitational acceleration

As a benchmark study with g = 9.800 m/s² as a standard case, Fig. 13 gave the numerical results of the relation between the displacement and gravitational acceleration for cases 1, 2, and 3, in the range of 9.780 m/s² –9.832 m/s² (the variation range on the earth). For case 1, the system lost its stability at 9.800 m/s², resulting in a snap-through displacement. Therefore, the displacement-gravitational acceleration curve became discontinuous. One gravitational acceleration (g = 9.800 m/s²) would correspond to two distinct displacements, which was unacceptable for a relative gravimeter. For case 2, the displacement showed a highly nonlinear dependency on the gravity acceleration, especially in the region near 9.800 m/s² (zero-stiffness point). So, it was hard to experimentally calibrate the accurate relation between the displacement and gravitational acceleration in such a highly nonlinear region near the zero-stiffness point, which was unfavorable for a relative gravimeter. Different from mode 1 and mode 2, a perfect linear relationship between the displacement and gravitational acceleration can be achieved for case 3. The displacement increased linearly with the gravitational acceleration with a positive slope (here, 1231 μm/ms⁻²). This meant a stable high mechanical sensitivity (0.012 nm/ng) of the beam-mass system can be obtained in

Fig. 12. The resonance frequency evolving with tilt angle for: (a) case 1, (b) case 2 and (c) case 3.

the range of 9.780–9.832 m/s^2. Such a design would be sufficient to recognize the variation of gravitational acceleration in the order of nano-g. For a relative gravimeter, the gravity acceleration was calculated according to the measured displacement increment caused by gravity variation. Thus, a linear relationship between the displacement and gravity acceleration was preferred.

4.4. Discussion

With small changes in the geometrical parameters of the beam-mass system studied here, we have shown the existence of three distinct deformation modes. For mode 1 and mode 2, a zero resonance frequency was theoretically available. However, both of them presented a very sensitive region where a tiny perturbation would result in a rapid change in resonance frequency. This means a tiny fabrication deviation would render a much higher resonance frequency. This would be the reason why it was so difficult to make a gravimeter with a resonance frequency lower than 1 Hz. As for mode 3, it provided a stable resonance frequency and linear relationship between the displacement and gravitational acceleration. So, to achieve a stable and ultra-low resonance frequency, the following guidelines were proposed,

Firstly, the buckling and zero-stiffness point should be prevented in the working region. The deformation mode with positive stiffness can be adopted to obtain a stable resonance frequency.

Secondly, to achieve a stable and ultra-low resonance frequency, the beam-mass structure should be further optimized to make its force–displacement curve have a wide flat region with constant and ultra-small slope, as schematically shown in Fig. 14. The near-zero but positive slope in a wide flat region will ensure that the beam-mass structure could maintain a stable and sensitive relationship between the gravitational acceleration and displacement in a wide working range of gravitational acceleration.

Thirdly, in our study, we only focused on three different deformation modes, but we did not study the desired tilt angle. In general, the device would work in an entire range of tilt angle until 90° to the vertical direction without failure. This means that a near-zero but positive slope in a wide flat region would be preferred near vertical direction.

5. Conclusions

In this paper, a detailed modeling study of buckling/non-buckling mechanical behavior was performed based on a four-beam mass MEMS device prototype. The numerical results for the resonance frequency and buckling threshold conditions were in good agreement with the experimental data. Subsequently, through the validated nonlinear finite element analysis, we investigated three different cases with three distinct modes of deformations. The results revealed that both the buckling mode and the zero-stiffness point mode present sensitive regions of system instability. On the other hand, the mode without both buckling and zero-stiffness point provided the beam-mass structure with a stable linear relationship between the displacement and gravitational acceleration. A near-zero and stable resonance frequency can be achieved with an optimized beam-mass structure, in which the force–displacement curve has a flat region with a constant and ultra-small slope. In addition, achieving a "flat region" with constant and ultra-small slope near vertical position is also part of the optimized design. Future work will be conducted to quantify the sensitivity of resonance frequency to each design parameter including beam thickness and tilt positions.

The authors declare that they have no known competing financial interests or personal relationships that could have appeared to influence the work reported in this paper.

References

[1] M.N. Nabighian, M.E. Ander, V.J.S. Grauch, R.O. Hansen, T.R. LaFehr, Y. Li, W.C. Pearson, J.W. Peirce, J.D. Phillips, M.E. Ruder, Historical development of the gravity method in exploration, Geophysics 70 (6) (2005) 63ND–89ND, https://doi.org/10.1190/1.2133785.

[2] B. Fores, C. Champollion, N.L. Moigne, R. Bayer, J. Chery, Assessing the precision of the iGrav superconducting gravimeter for hydrological models and karstic hydrological process identification, Geophys. J. Int. 208 (2017) 269–280. doi:10.1093/gji/ggw396.

[3] G. Kaufmann, Geophysical mapping of solution and collapse sinkholes, J. Appl. Geophy. 111 (2014) 271–288, https://doi.org/10.1016/j.jappgeo.2014.10.011.

[4] M. Van Camp, O. de Viron, A. Watlet, B. Meurers, O. Francis, C. Caudron, Geophysics from terrestrial time-variable gravity measurements, Rev. Geophys. 55 (4) (2017) 938–992, https://doi.org/10.1002/2017RG000566.

[5] C. Wang, F. Chen, Y. Wang, S. Sadeghpour, C. Wang, M. Baijot, R. Esteves, C. Zhao, J. Bai, H. Liu, M. Kraft, Micromachined accelerometers with sub-μg/√Hz noise floor: a review, Sensors 20 (14) (2020) 4054, https://doi.org/10.3390/s20144054.

[6] U. Krishnamoorthy, R.H. Olsson, G.R. Bogart, M.S. Baker, D.W. Carr, T.P. Swiler, P.J. Clews, In-plane MEMS-based nano-g accelerometer with sub-wavelength optical resonant sensor, Sens. Actuators A Phys. 145-146 (2008) 283–290, https://doi.org/10.1016/j.sna.2008.03.017.

[7] M. Zhang, J. Liu, S. Tang, L. Tu, Cross-axis sensitivity calibration of MEMS gravimeters on a dividing head, in: 2020 IEEE Int. Symp. Inertial Sens. Syst. (INERTIAL), Hiroshima, Japan, March. 2020, pp. 1–4. doi:10.1109/INERTIAL48129.2020.9090076.

[8] L. Timmen, in: Sciences of Geodesy - I, Springer Berlin Heidelberg, Berlin, Heidelberg, 2010, pp. 1–48, https://doi.org/10.1007/978-3-642-11741-1_1.

[9] S. Tang, H. Liu, S. Yan, X. Xu, L. Tu, A MEMS gravimeter qualified for earth tides measurement, in: Proc. 20th Int. Conf. Solid-State Sens. Actuators Microsyst. Berlin, Germany, pp. 499-502, Jun. 2019, doi:10.1109/TRANSDUCERS.2019.8808444.

[10] J. Laine, D. Mougenot, A high-sensitivity MEMS-based accelerometer, Lead. Edge 33 (11) (2014) 1234–1242, https://doi.org/10.1190/tle33111234.1.

[11] W.J. Wu, D. Liu, W. Qiu, H. Liu, F. Hu, J. Fan, C. Hu, L. Tu, A precise spacing-control method in MEMS packaging for capacitive accelerometer applications, J. Micromech. Microeng. 28 (2018) 125016, https://doi.org/10.1190/tle33111234.1.

[12] S. An, K. Bongsu, K. Soyoung, M. Geol, L. Manhee, J. Wonho, Buckling-based non-linear mechanical sensor, Sensors 18 (2018) 2637, https://doi.org/10.3390/s18082637.

[13] G. Cella, V. Sannibale, R. DeSalvo, S. Márka, A. Takamori, Monolithic geometric anti-spring blades, Nucl. Instrum. Methods Phys. Res. A 540 (2-3) (2005) 502–519, https://doi.org/10.1016/j.nima.2004.10.042.

[14] R.P. Middlemiss, A. Samarelli, D. J. Paul, J. Hough, S. Rowan, G. D. Hammond, Measurement of the Earth tides with a MEMS gravimeter, Nature 531 (2016) 614–617. doi:10.1038/nature17397.

[15] R.P. Middlemiss, S.G. Bramsiepe, R. Douglas, S. Hild, J. Hough, D.J. Paul, A. Samarelli, S. Rowan, G.D. Hammond, Microelectromechanical system gravimeters as a new tool for gravity imaging, Philos. Trans. A Math. Phys. Eng. Sci. 376 (2120) (2018) 20170291, https://doi.org/10.1098/rsta.2017.0291.

[16] A. Prasad, S.G. Bramsiepc, R.P. Middlemiss, J. Hough, D.J. Paul, A portable MEMS gravimeter for the detection of the earth tides, in: Proc. IEEE Sensors 2018, New Delhi, India, Oct. 2018, pp. 1–3. doi:10.1109/ICSENS.2018.8589884.

[17] H. Droogendijk, Design and fabrication of a bulk micromachined accelerometer for geophysical applications, M.S. thesis, Dept. Elect. Eng. Univ. Twente, Enschede, the Netherlands, 2009.

[18] Z. Li, W. Wu, P. Zheng, J. Liu, J. Fan, L. Tu, Novel capacitive sensing system design of a microelectromechanical systems accelerometer for gravity measurement applications, Micromachines 7 (2016) 167, https://doi.org/10.3390/mi7090167.

[19] S. Tang, H. Liu, S. Yan, X. Xu, W. Wu, J. Fan, J. Liu, C. Hu, L. Tu, A high-sensitivity MEMS gravimeter with a large dynamic range, Microsyst. Nanoeng. 5 (2019) 1–11, https://doi.org/10.1038/s41378-019-0089-7.

[20] W. Wu, D. Liu, H. Liu, S. Yan, S. Tang, J. Liu, F. Hu, J.i. Fan, L. Tu, Measurement of tidal tilt by a micromechanical inertial sensor employing quasi-zerostiffness mechanism, J. Microelectromech. Syst. 29 (5) (2020) 1322–1331, https://doi.org/10.1109/JMEMS.2020.3001928.

[21] B. El Mansouri, L.M. Middelburg, R.H. Poelma, G.Q. Zhang, H.W. van Zeijl, J. Wei, H. Jiang, J.G. Vogel, W.D. van Driel, High-resolution MEMS inertial sensor combining large-displacement buckling behaviour with integrated capacitive readout, Microsyst. Nanoeng. 5 (1) (2019), https://doi.org/10.1038/s41378-019-0105-y.

[22] M.A. Hopcroft, W.D. Nix, T.W. Kenny, What is the Young's Modulus of Silicon, J. Microelectromech. Syst. 19 (2) (2010) 229–238, https://doi.org/10.1109/JMEMS.2009.2039697.

[23] E. Riks, An incremental approach to the solution to the solution of buckling and snapping problems, Int. J. Solids Struct. 15 (1979) 524–551, https://doi.org/10.1016/0020-7683(79)90081-7.